



# The electrostatic plasma environment of a small airless body under non-aligned plasma flow and UV conditions

A.R. Poppe<sup>a,e,\*</sup>, M.I. Zimmerman<sup>b,e</sup>, J.S. Halekas<sup>c,e</sup>, W.M. Farrell<sup>d,e</sup>

<sup>a</sup> Space Sciences Laboratory, 7 Gauss Way, University of California at Berkeley, Berkeley, CA 94720, USA

<sup>b</sup> Johns Hopkins University Applied Physics Laboratory, Laurel, MD 20723, USA

<sup>c</sup> Department of Physics and Astronomy, University of Iowa, Iowa City, IA, USA

<sup>d</sup> NASA Goddard Space Flight Center, Greenbelt, MD 20771, USA

<sup>e</sup> Solar System Exploration Research Virtual Institute, NASA Ames Research Center, Mountain View, CA, USA

## ARTICLE INFO

### Article history:

Received 4 December 2014

Received in revised form

13 May 2015

Accepted 2 June 2015

Available online 11 June 2015

### Keywords:

Surface charging/potentials

Airless bodies

Plasma interactions

Plasma wakes

Photoelectron sheaths

## ABSTRACT

Airless bodies interact with a wide variety of plasma environments throughout the solar system. For many objects, incident plasma is nearly co-aligned with solar ultraviolet radiation leading to the development of a positively charged dayside photoelectron sheath and a negatively charged nightside plasma sheath. Other objects, however, are present in environments where the plasma flow and solar UV radiation may not co-align. These environments include, for example, the moons of Mars as they pass through the deflected Martian magnetosheath, and many of the moons of the outer planets, which are embedded in co-rotating planetary magnetospheres. The decoupling of the plasma flow and UV incidence vectors opens up a wide range of possible surface charging and near-object plasma conditions as a function of the relative plasma-UV incidence angle. Here, we report on a series of simulations of the plasma interaction of a small body (effectively smaller than both electron and ion gyroradii) with both flowing plasma and UV radiation for different plasma-UV incidence angles using an electrostatic treecode model. We describe the plasma and electric field environment both on the object surface and in the interaction region surrounding the object, including complex surface charge and electric field distributions, interactions between surface-generated photoelectrons and ambient plasma electrons, and complex potential distributions, all of which vary as a function of the relative plasma flow-UV angle. We also show that in certain conditions, non-monotonic potential structures may exist around such objects, partially similar to those found at Earth's Moon.

© 2015 Elsevier Ltd. All rights reserved.

## 1. Introduction

Objects without a thick atmosphere and global magnetic field, such as asteroids or planetary satellites at Earth, Mars, and the outer planets, have surfaces directly exposed to ambient plasma and fields. This results in several processes including the formation of a downstream wake (for flowing ambient plasmas) (e.g., Halekas et al., 2014), surface charging (Whipple, 1981), and the production and ionization of tenuous neutral exospheres (e.g., Wurz et al., 2007). Surface charging, for example, has been thoroughly investigated at Earth's Moon in several different plasma environments, including the solar wind, terrestrial magnetosheath, and terrestrial magnetotail. In situ observations by both the Lunar Prospector spacecraft (Halekas et al., 2005b, 2008, 2012) and the Acceleration, Reconnection, Turbulence, and Electrodynamics of

the Moon's Interaction with the Sun (ARTEMIS) mission (Halekas et al., 2011; Poppe et al., 2012a) have inferred the surface potential of the Moon via electron reflectometry (Anderson et al., 1976), whereby electrostatic and surface magnetic fields alter and partially reflect incident electron fluxes and, in some cases, accelerate surface-originating electrons (generated by a combination of photo- and secondary emission) away from the surface. Based on these observations, along with theoretical and modeling work, we know that in the solar wind the Moon typically charges positive on the dayside to potentials < 10 V, while on the nightside, the lack of photoemission, rarified plasma densities in the wake, and elevated electron temperatures (Halekas et al., 2005a,b) induce surface potentials ranging from hundreds of Volts negative during typical solar wind conditions to greater than −4.5 kV during solar energetic events (Halekas et al., 2007). Lunar surface charging in the terrestrial magnetotail is more varied due to the wider range of plasma parameters present. Surface potential measurements in the plasma sheet have found potentials up to −500 V on the dayside (Halekas et al., 2008; Poppe et al., 2011, 2012a), while

\* Corresponding author.

E-mail address: [poppe@ssl.berkeley.edu](mailto:poppe@ssl.berkeley.edu) (A.R. Poppe).

other observations suggest that potentials can reach +40 V or higher on the dayside while in the magnetotail lobe (Tanaka et al., 2009; Poppe et al., 2013; Harada et al., 2013). Finally, recent measurements of surface charging at Saturn's small moon Hyperion by the Cassini spacecraft have inferred a –200 V surface potential, in accordance with theoretical current balance calculations (Roussos et al., 2010; Nordheim et al., 2014).

Much work has also been dedicated to the study of plasma wakes formed behind airless objects. Theoretical expressions for the behavior of a plasma as it refills the void left by an object have been developed for a range of increasing complexity, spanning the assumption of quasi-neutral plasma with cold ions (Gurevich et al., 1969; Gurevich and Pitaevskii, 1975; Samir et al., 1983) to arbitrary electron and ion distributions (Halekas et al., 2005a, 2014). More sophisticated, multi-dimensional simulations have also explored plasma wakes at airless bodies, including magnetohydrodynamic (Xie et al., 2013), hybrid (Trávníček et al., 2005; Kallio, 2005; Roussos et al., 2008; Simon et al., 2009; Holmström et al., 2012; Fatemi et al., 2013), and kinetic models (Farrell et al., 1998; Birch and Chapman, 2001b, 2001a; Nakagawa and Kimura, 2011; Nakagawa, 2013). Many of these theories and simulations have been compared to various in situ data at Earth's Moon from WIND (Ogilvie et al., 1996), Lunar Prospector (Halekas et al., 2005b), or ARTEMIS (Halekas et al., 2014; Poppe et al., 2014) or at various moons of Saturn with Cassini (Roussos et al., 2008; Simon et al., 2009) with good agreement.

While most airless bodies in the solar system are embedded in environments such as the solar wind where the plasma flow and solar ultraviolet irradiation are nearly aligned, not all objects fall into such a category. The largest group of objects that experiences non-aligned plasma flow/UV irradiation is the various moons of the outer planets, many of which are embedded within rotating planetary magnetospheres. As these moons orbit their parent planet, the azimuthally rotating plasma and the constant ultraviolet irradiation sweep out a full range of relative angles. A theoretical investigation of the charging environment of Saturn's large, icy, non-conducting moons, Rhea, Tethys, Dione, and Mimas, found that significant changes in the near-surface electrostatic environment of the upstream hemisphere each of these moons could be induced by changing the relative UV/plasma flow angle (Roussos et al., 2010). Such non-aligned environments may also be found at the Martian moons, Phobos and Deimos, when they transit through the shocked and deflected magnetosheath of Mars. Finally, non-aligned environments can be found at Earth's Moon during its periodic transit through the terrestrial magnetotail, where plasma has been observed with significant lateral and/or earthward flow. For example, Harada et al. (2010) inferred the presence of surprisingly strong electric fields of  $\approx 10$  mV/m (compared to typical magnetotail convection electric fields of 0.5–2 mV/m McCoy et al., 1975) near the limb of the lunar surface with lateral convection while in the terrestrial magnetotail, yet the mechanism by which these electric fields are created is not currently understood and could be related to offsets between UV photoemission and plasma flow. At each of these bodies, the interaction of ambient flowing magnetospheric plasma on both the upstream and downstream hemispheres with solar UV-induced photoelectrons may result in complex charging, electrostatic potential, and electric field distributions both on and around the object.

In this paper, we explore the electrostatic environment of an object in a flowing plasma with varying illumination and plasma flow angles using an electrostatic kinetic treecode model (Zimmerman et al., 2014). In Section 2, we describe the model while Section 3 presents the simulation results. Finally, in Section 4 we discuss our findings, in particular how our results may apply

in situations where the various ratios of the object radius to plasma scales are much larger, and outline future work.

## 2. Model

In order to model the electrostatic environment around small objects with non-aligned plasma flow and solar UV irradiation, we have used a kinetic, electrostatic treecode (Zimmerman et al., 2014), similar in many ways to standard particle-in-cell (PIC) codes that have been extensively used in modeling plasma environments (e.g., Birdsall and Langdon, 1985). An arbitrary number of ion and electron species are kinetically tracked within a two-dimensional domain under Lorentz motion and are allowed us to enter and leave the simulation domain as well as collect on surfaces within the domain. Computation of the electric field in the simulation is performed through a combination of two methods: (1) the particles are collected into small clusters (or “leaves”) and mutual electrostatic fields between leaves are determined by a multipole expansion and (2) in order to maintain accuracy at small scales, direct Coulomb's law calculations are performed for particles within a given leaf. The adaptation of treecodes – originally developed to simplify  $O(N^2)$  gravitational forces in astrodynamical simulations (Barnes and Hut, 1986) – for electrostatic physics has been outlined by Christlieb et al. (2006), whose formulation was followed in designing and implementing the treecode. One major advantage of the treecode over a traditional PIC code is the ability to resolve arbitrarily small length scales in high-density (i.e., small Debye length) regions without having to implement a domain-wide, high-resolution grid or conformal mapping (which is computationally intensive). The treecode naturally solves this problem by creating more and smaller clusters of particles within high-density regions in order to provide adequate resolution. First results from the treecode have focused on the complex charging environment on and around an irregularly-shaped asteroid in the solar wind (Zimmerman et al., 2014) and have demonstrated the capability to efficiently and accurately model electrostatic environments under complex plasma and UV illumination geometries.

Given the wide range of ambient plasma parameters that occur throughout the solar system, a full understanding of the plasma environment(s) for non-aligned plasma flow/UV conditions across all relative plasma scale lengths is beyond the scope of this paper; therefore, for this study, we have selected a single case of plasma parameters meant to approximate that encountered in planetary magnetospheric environments such as Saturn and have varied only the plasma flow/UV illumination angle. While the treecode has the ability to include static magnetic fields and 2.5-dimensional gyro-motion, we do not include any magnetic fields at present as the object scale size is significantly smaller than typical ion and electron gyro-radii. Table 1 details the parameters chosen for this study, along with several derived quantities. While these parameters are not exactly that encountered at any specific object, they nonetheless provide a useful case for studying non-aligned

**Table 1**

Plasma parameters and selected derived quantities for the electrostatic treecode simulations presented here.

Parameter	Values
Plasma bulk velocity	100 km/s
Ambient plasma density	$5 \times 10^6 \text{ m}^{-3}$
Photoelectron density at surface, $0^\circ$ case	$10^7 \text{ m}^{-3}$
Proton, electron, photoelectron temperatures	10, 10, 2 eV
Object radius/ambient Debye length ( $R_m/\lambda_D$ )	$\approx 20$
Simulation timestep	$5 \times 10^{-7} \text{ s}$
Number of simulation particles	$> 10^6$

plasma/illumination environments, especially as these parameters are relevant to the study of objects embedded in co-rotating magnetospheres of the outer planets, where non-aligned plasma/illumination is a basic feature (e.g., Roussos et al., 2010; Nordheim et al., 2014). Particle populations in the model include ambient protons (at realistic proton mass), ambient electrons, and surface-originating photoelectrons. We place a single spherical (truly cylindrical in two dimensions) object in the plasma flow, leaving the study of more complex surface topography under non-aligned conditions to future work (e.g., Poppe et al., 2012b; Zimmerman et al., 2014). In order to model the object as an insulator, the surface is composed of 250 discrete elements, each of which separately tracks the number of collected and emitted particles (i.e., both ambient plasma and photoelectrons). The electrostatic field from this surface charge is included in calculations of the electric force on all particles in the simulation. Photoemission from the surface is controlled by an overall photoemission rate (see Table 1); an appropriate number of photoelectrons are stochastically emitted from each object element according to this rate. The plasma flow/UV illumination angle is set at three values: 0°, 90°, and 180°. As shown in the diagram in Fig. 1, the plasma flow direction in the simulation is kept constant (left-to-right) while the illuminated hemisphere is rotated to the chosen angles. Each model run contains sufficient number of macroparticles (typically on the order of  $10^6$ ) to ensure adequate statistics. Protons and electrons are pre-loaded in the simulation with specified densities and the simulation is run past the point that equilibrium is reached. Results following equilibrium are averaged together to obtain improved statistics.

### 3. Results

#### 3.1. Densities

Fig. 2 shows the relative proton, electron, and photoelectron densities for the three modeled cases of UV/plasma flow alignment, respectively. In all three cases, a plasma void in the ambient electrons and ions extends downstream from the object as plasma is absorbed on the upstream hemisphere, Fig. 2(a)–(f). Rarefaction waves in the ambient plasma density can be seen propagating outwards from the body at approximately the ion sound speed while convecting downstream. The photoelectron density, Fig. 2

(g)–(i), changes significantly as a function of the plasma flow/illumination angle. For 0°, Fig. 2(g), the photoelectron sheath extends far out into the upstream plasma flow, with a roughly cosine solar zenith angle dependence. A correlated decrease in the ambient electron density upstream of the body is also seen, Fig. 2(d), as approaching electrons are accelerated by the positive photoelectron sheath potential into the surface similar to that seen in one-dimensional theory (Nitter et al., 1998) and PIC simulations (Poppe and Horányi, 2010, Fig. 2). For 90°, Fig. 2(h), the photoelectron sheath spans part of both the upstream and downstream hemispheres. The upstream half of the photoelectron sheath resembles the aligned, 0° case with a cosine solar zenith angle dependence, while the downstream portion of the photoelectron sheath is much thinner. Finally, in Fig. 2(i), the photoelectron sheath on the downstream hemisphere, 180°, is significantly different from that found for the 0° case. The photoelectrons preferentially leak away from the surface along the flanks, forming a pair of broad, tenuous electron beams (labeled in Fig. 2(i)), while the sheath is thinnest in the center of the wake where the ambient electron current to the surface is lowest. Such behavior in the photoelectrons is similar to that explored previously at the Moon during various stages of a coronal mass ejection with a series of particle-in-cell codes (Farrell et al., 2013). These simulations found that the nature of the photoelectron sheath can be characterized by the ratio of emitted photoelectron current,  $J_{ph}$ , to the collected electron current,  $J_e$ . During times when  $J_{ph}/J_e > 1$ , the surface charged positively and effectively trapped most photoelectrons just above the surface whereas in contrast, when  $J_{ph}/J_e < 1$ , the incoming plasma electron current allowed a greater fraction of photoelectrons to escape the surface.

The difference in the photoelectron sheath thickness as a function of solar zenith angle between the three cases is not only controlled by the balance of incoming and outgoing currents but also is driven by changes in the effective electron temperature near the surface. As detailed by Grard and Tunaley (1971), many photoelectron sheath parameters are governed by an effective electron Debye length:

$$\lambda_o = \sqrt{\frac{\epsilon_o m_e v_e^2}{n_o e^2}}, \quad (1)$$

where  $\epsilon_o$  is the permittivity of free space,  $m_e$  is the electron mass,  $n_o$  is the electron density near the surface,  $e$  is the elementary charge, and  $v_e$  is the mean electron velocity given by

$$v_e = \int_0^\infty v_o^2 f(v_o) dv_o, \quad (2)$$

where  $f(v_o)$  is the electron velocity distribution near the surface. For the 0° case, the presence of inflowing ambient electrons, whose temperature is greater than that of the photoelectrons, raises the effective electron temperature near the surface yielding a relatively larger  $\lambda_o$ . For the 90° and 180° cases, the respective portions of the photoelectron sheath that are immersed in the object wake have less ambient electron inflow and thus, both  $v_e$  and  $\lambda_o$  are smaller. This translates into a thinner photoelectron sheath along portions of the surface exposed to the object's plasma wake.

The simulation results also suggest that changes in the relative illumination angle – which controls the presence of photoelectrons only – can alter the global structure of the wake, at least for small objects. Fig. 3 shows the ratio of the proton densities for (a) 90° and (b) 180°, respectively, to the proton density for 0°. Far from the object, the density between all three cases is the same; however, significant deviations are seen on the object flanks and in the wake as the UV illumination is rotated. For 90° illumination, higher relative proton density is seen on the illuminated flank and

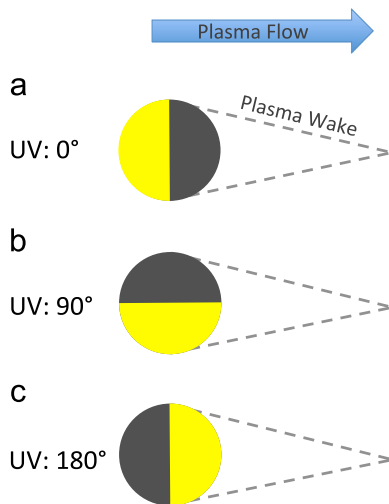
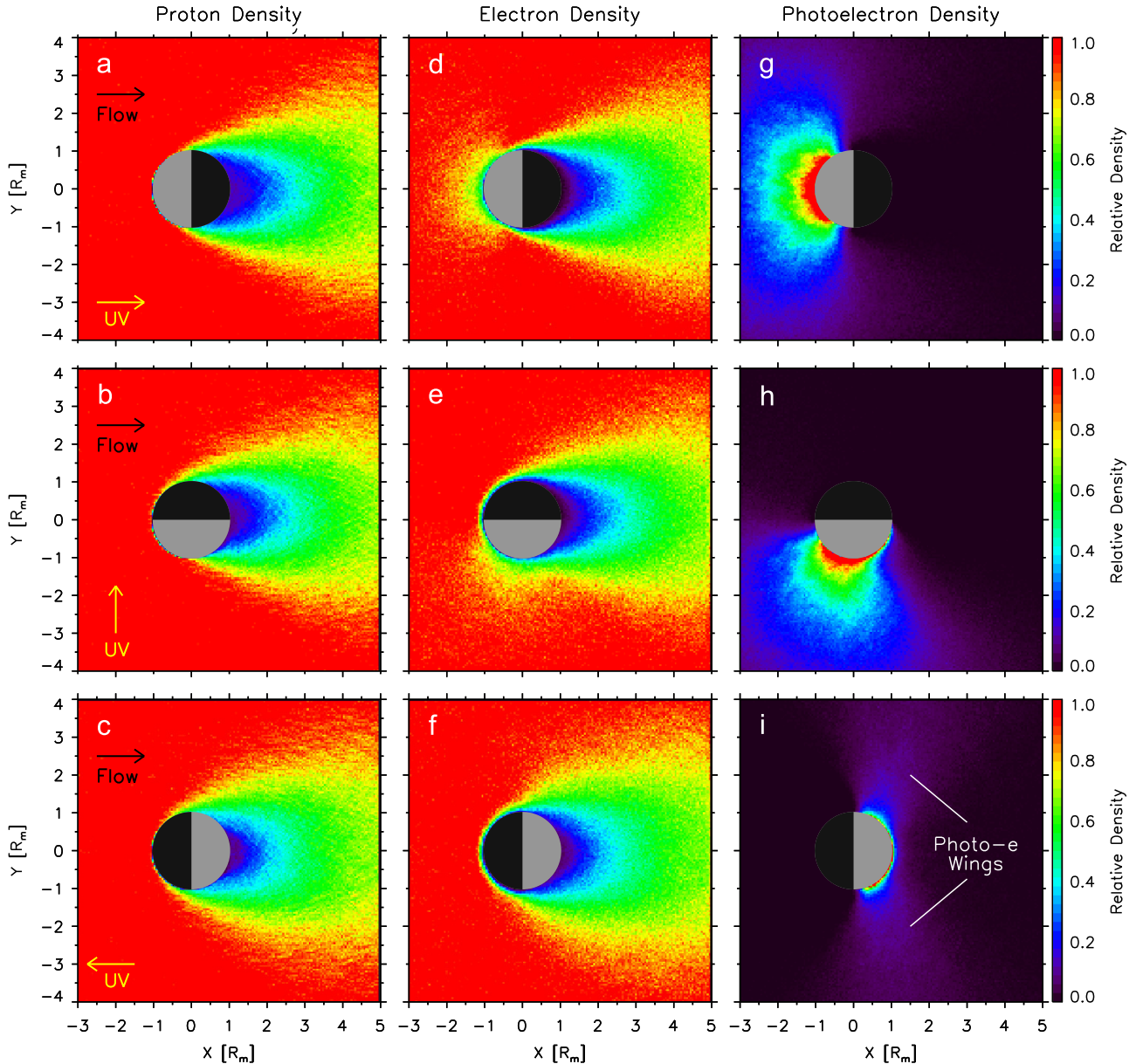


Fig. 1. A cartoon of the plasma flow/UV geometry simulated here: (a) 0°, (b) 90°, and (c) 180°. Note that the plasma flow direction in the simulation (and all plots shown here) is kept constant (left-to-right).



**Fig. 2.** The proton, electron, and photoelectron densities for the three alignment cases. The arrows in (a)–(c) denote the flow and UV directions for each case, respectively.

downstream into the wake while the un-illuminated side has a relatively lower density. The  $180^\circ$  case shows several features (labeled in Fig. 3(b)) including: (1) a large deficit in the proton density in the deepest plasma void just above the surface ( $x \approx 1.0 - 1.2 R_m$ ), (2) an increase in relative proton density within the plasma wake starting from the flanks and moving inwards, and (3) two “wings” of lower density starting from the upstream hemisphere and propagating out into the ambient plasma. These changes in relative densities are due to interactions between the flowing protons and the differing electric fields either on the surface or in the wake of the object.

To further elucidate this effect, Fig. 4(a) and (b) shows the proton phase space as a function of cross-wake distance,  $y$ , along a cut from 1 to  $1.25 R_m$  downstream of the object (denoted in Fig. 3 by the pair of vertical dotted lines). The colored symbols (red, blue) are for the respective non-aligned cases ( $90^\circ$  and  $180^\circ$ ) while the black symbols on both panels are for the aligned,  $0^\circ$  case. Between approximately  $-1$  and  $1 R_m$  the plasma wakes in all cases are readily evident by the relative lack of particles and the presence of accelerated particles.

While the phase spaces far from the central wake are equivalent between the  $0^\circ$  case and the  $90^\circ$  and  $180^\circ$  cases, they differ inside the wake. For the  $90^\circ$  case, Fig. 4(a), protons entering from the left side of the wake ( $y < 0 R_m$ ) show no signs of acceleration as the  $0^\circ$  protons do. Protons entering from the right side of the wake, however, do show acceleration in both the  $0^\circ$  and  $90^\circ$  cases. For the  $180^\circ$  case, Fig. 4(b), protons entering both sides of the wake show no evidence of acceleration as the  $0^\circ$  case protons do.

The proton acceleration evident in the  $0^\circ$  case into the wake is typically induced by the presence of electrostatic ambipolar fields on the wake flanks, as suggested at Earth’s Moon and other airless bodies (Farrell et al., 1998; Birch and Chapman, 2001b; Nakagawa, 2013). These ambipolar fields are generated by a charge separation between electrons, which quickly rush to fill the plasma void, and ions, which refill the void at a slower rate due to their higher mass. Fig. 4(c) shows the electric field magnitude as a function of cross-wake distance,  $y$ , for all three simulation cases at the same downstream distance as Fig. 4(a) and (b). For the  $0^\circ$  case (black) the electric field is present at non-negligible levels within the

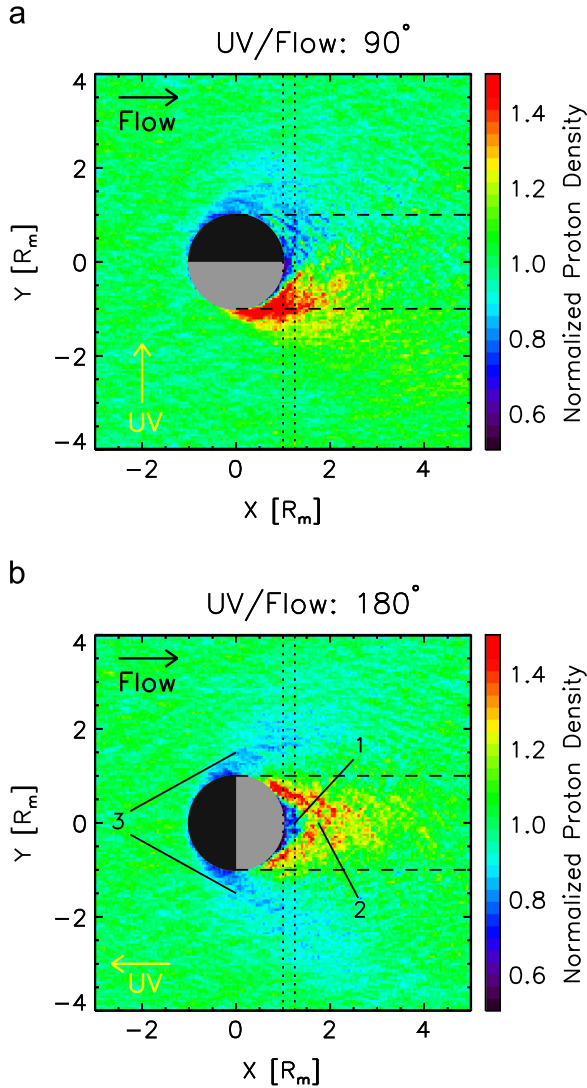


**Fig. 3.** The proton density for (a) 90° and (b) 180° relative to the 0° case. The vertical dotted lines indicate the slice plotted in Fig. 4 while the horizontal dashed lines mark the boundary of the plasma shadow, for reference. The numbers in (b) refer to features discussed in the text.

wake, between  $-1$  and  $1 R_m$ , at a maximum of approximately  $0.9$  V/m. The 90° case (blue) shows a nearly identical electric field for  $y > 0.2 R_m$ , a higher peak within the wake of approximately  $1.2$  V/m at  $y=0$ , and an essentially negligible level of electric field on the left side of the wake ( $y < 0$ ). Finally, the 180° case (red) shows no significant electric field across the entire wake along the chosen cut. The changes in the wake electric field and relative proton densities in the 90° and 180° cases are ultimately driven by the presence of photoelectrons emitted from the surface directly into the wake (cf., Fig. 2(i)). As these photoelectrons enter the wake and the wake flanks, they replace ambient electrons collected on the surface of the object and restore local quasi-neutrality, shorting out ambipolar electric fields along the wake flank. Without the ambipolar electric fields, the protons are not accelerated into wake, but rather enter similar to a simple gas-dynamic fashion.

### 3.2. Potentials and surface charge

Fig. 5(a)–(c) shows the two-dimensional electrostatic potential distribution for each of the three cases. All potentials are referenced to the average potential along the upstream boundary. In the 0°

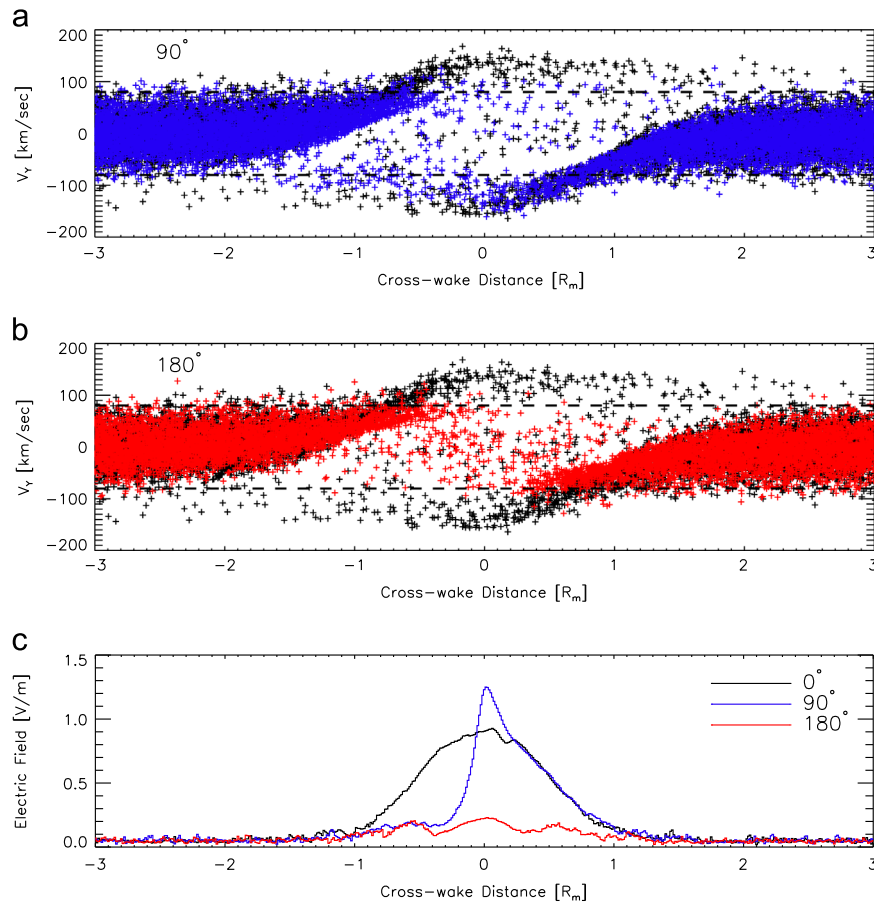
case, Fig. 5(a), potentials of approximately  $+5$  V and  $-50$  V are present on the upstream and downstream sides of the body, respectively, a configuration typical for aligned UV/flow conditions. In the 90° case, Fig. 5(b), positive potentials of  $\approx +10$  V are found on the dayside and  $-50$  V on the nightside, similar in magnitude to the 0° case however rotated along with the UV illumination. In the 180° case, Fig. 5(c), which is also shown expanded in Fig. 5(d), the potential structure is more complex. On the upstream, un-illuminated side, the potential forms an  $\approx -20$  V sheath while on the downstream, illuminated side of the object, the potential is non-monotonic with a surface potential of  $\approx -10$  V yet a minimum of  $-20$  V above the surface  $\approx 0.25 R_m$  downstream.

Fig. 6 shows the surface charge and surface potential (with respect to the potential at the upstream model boundary) as a function of sub-flow angle for all three cases. The yellow bar at the top of each panel denotes the region of UV illumination in each case. For the 0° case, the surface charge is slightly positive ( $\approx 5 \times 10^6$  electrons/m<sup>2</sup>) on the dayside and negative ( $\approx -15 \times 10^6$  electrons/m<sup>2</sup>) on the nightside. Surface potentials follow a similar pattern, with a 5 V maximum on the dayside and a  $-60$  V minimum on the nightside. Such a configuration is analogous to that found at Earth's Moon (Halekas et al., 2008). Surface charge and potentials for the 90° case are generally organized by the location of the UV irradiation (ranging from 0 to 180° sub-flow angles) with positive surface charge and potentials on the dayside of the object and negative surface charges and potentials on the nightside of the object, despite the offset with respect to the flow direction. The magnitude of the surface charge and potential on the dayside are slightly higher for the 90° case than for the dayside in the 0° case. The lowest potential is still found at the anti-flow location (sub-flow angle =  $\pm 180^\circ$ ) at approximately  $-60$  V. We do note that the surface charge experiences a sharp jump across the anti-flow location from a surface charge of  $\approx 15 \times 10^6$  electrons/m<sup>2</sup> at sub-flow angles of 170 to 180° to  $\approx -30 \times 10^6$  electrons/m<sup>2</sup> at sub-flow angles of  $-170$  to  $-180^\circ$ . This point marks one of the sunlight/shadow boundaries for the 90° case. Such a sharp transition in the surface charge generates a strong local, horizontal electric field at this point on the object.

The surface charge and potential for the 180° case are more complex than either of the 0° or 90° cases, due to the anti-alignment of the plasma flow and the UV irradiation. The upstream hemisphere of the object (sub-flow angles  $-90$  to  $90^\circ$ ) has both negative surface charge and potential as expected for a surface exposed to only ambient plasma (i.e., no photoemission). Surface charges are approximately  $-20 \times 10^6$  electrons/m<sup>2</sup> and the surface potential ranges between  $-30$  and  $-20$  V. The opposite hemisphere of the object, dayside yet anti-flow, has a fairly high surface charge,  $\approx 10 \times 10^6$  electrons/m<sup>2</sup>, due to the high photoemissive current relative to the fairly tenuous ambient electron current from the object's wake. The potential on this hemisphere, however, remains either at or below zero with respect to the outer boundary. Such a configuration, positive surface charge yet negative surface potential, is indicative of the presence of a non-monotonic potential structure above the surface, analogous to that simulated and observed at Earth's Moon (e.g., Poppe and Horányi, 2010; Poppe et al., 2011; Halekas et al., 2011) and as noted earlier in the two-dimensional potential distributions (cf., Fig. 5(d)).

### 3.3. Surface electric fields

Finally, Fig. 7 shows the electric fields on the surface of the object for each case, broken down by the magnitude as well as the local radial and tangential components. For the 0° case, Fig. 7(a), the surface electric field is exclusively positive and radial at



**Fig. 4.** The  $v_y$ - $y$  phase space for (a) the 90° case and (b) the 180° case along the region denoted by the dotted lines in Fig. 3. Plotted in black on both (a) and (b) is the phase space for the 0° case. Additionally, the horizontal dashed lines mark the edge of the approximate maximum ion velocities in the gas-dynamic solution, for comparison to the ambipolar accelerated ions. (c) The electric field magnitude across the wake for all three cases for the same region. (For interpretation of the references to color in this figure caption, the reader is referred to the web version of this paper.)

maximum strengths of  $\approx 0.5$  V/m for sub-flow angles less than  $\approx 45^\circ$  (i.e., in the center of the dayside photoelectron sheath), while transitioning to negative, stronger radial fields (maximum of  $\approx 2$  V/m) for the rest of the object. Small tangential electric fields (red) are present at both terminators (sub-flow angles =  $90^\circ$ ). Overall, the largest electric fields on the surface of the object for this case occur right at the terminators. For the 90° case, Fig. 7(b), the surface electric field is mainly positive and radial for the illuminated portion of the surface (sub-flow angles from  $45^\circ$  to  $180^\circ$ ) and negatively radial for the rest of the surface. As noted earlier, an important exception in this case is the presence of a strong, localized electric field, comprised of both radial and tangential components at the anti-flow point (sub-flow angles of  $-180/180^\circ$ ), correlated with a sharp change in the surface charge density from positive (in sunlight) to negative (in shadow). The electric field magnitude seen here is the highest in all simulations at approximately 2.5 V/m. For the 180°, Fig. 7(c), the surface electric fields are radial and negative for sub-flow angles less than  $100^\circ$  (as ambient electron collection outweighs photoemission) and positive and radial for the anti-flow hemisphere, which is in sunlight. We also note small ( $\approx 0.5$  V/m) tangential electric fields at sub-flow angles of  $\pm 90^\circ$ , similar to those seen in the 0° case. At certain locations in each of the modeled cases, we also note points where the surface electric field reaches a minimum, often close to zero (denoted in Fig. 7 with the solid triangles). Similar locations have been noted in a previous theoretical study of the surface charging of Saturn's moons (Roussos et al., 2010) and at Earth's Moon (Farrell et al., 2007). Such minima in surface electric fields have often been studied from the perspective of electrostatic dust

charging, levitation, and possible escape from airless bodies as locations where no such levitation could occur. Our simulations here suggest that the presence of these locations persist under varying solar UV/plasma flow alignment, although, not without some change. The 90° case has only one such point at a sub-flow angle of  $45^\circ$  as opposed to the pair of locations seen for the 0° and 180° cases, and the locations of the minima in the 180° are farther from the sub-UV point than for the 0 and 90° cases (approximately  $75^\circ$  solar zenith angle as opposed to  $45^\circ$  solar zenith angle).

#### 4. Discussion and conclusion

We have presented simulations of the electrostatic environment around a small, airless body in a flowing plasma under conditions of both aligned and non-aligned flow and UV irradiance. The use of the newly-developed electrostatic treecode (Zimmerman et al., 2014) is well-suited to studying surface-plasma interactions at small, kinetic scales where both electron and ion dynamics must be resolved. This is especially important for understanding the kinetic interaction in the sheath region around the object as the relative photoemission and plasma collection currents vary with respect to one another. The treecode also allows a self-consistent simulation of the interaction between the sheath region and the object wake, where, at least for small objects, these two plasma structures may partially merge and/or interact with one another. While the simulations presented here are two-dimensional, and thus, do not capture the full, three-

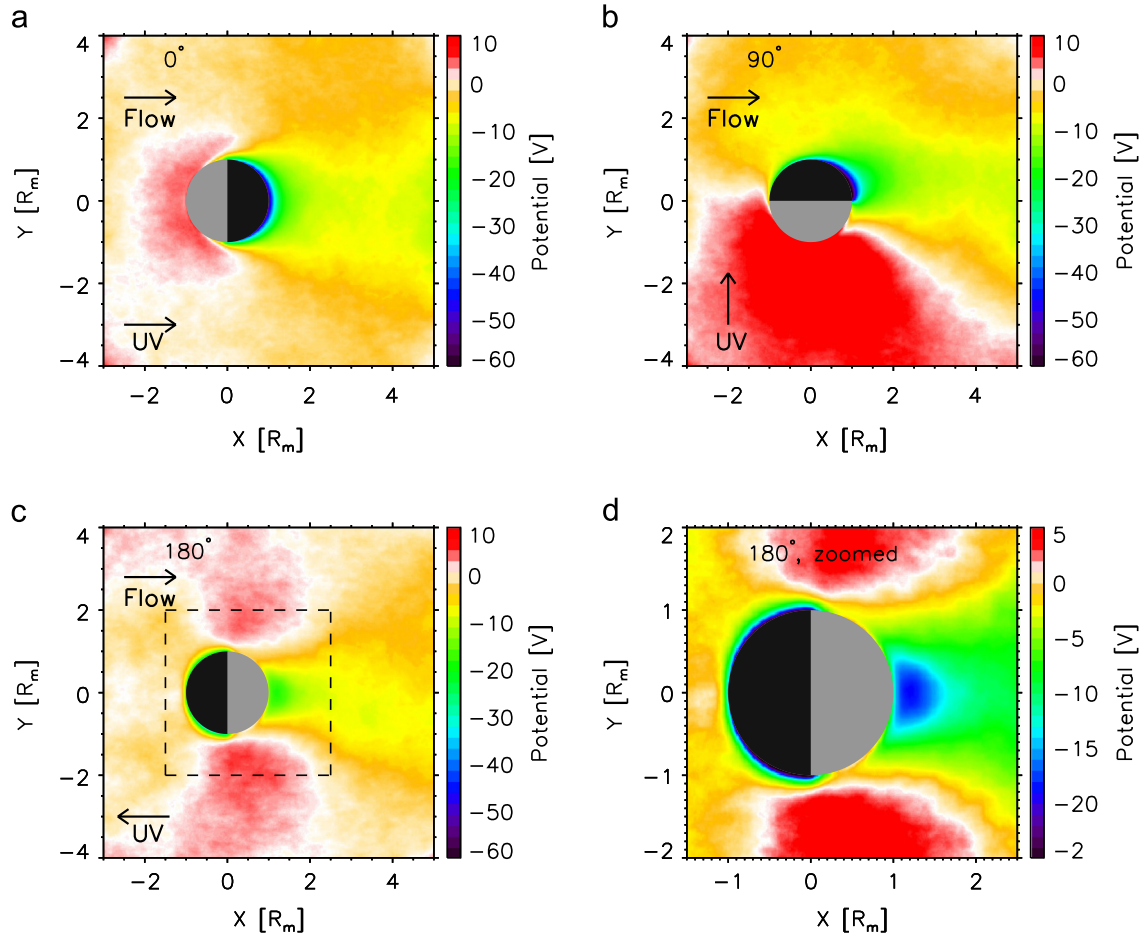


**Fig. 5.** The electrostatic potential for UV/plasma flow angles of (a)  $0^\circ$ , (b)  $90^\circ$ , and (c)  $180^\circ$ . (d) The electrostatic potential for the  $180^\circ$  case zoomed in and re-scaled to highlight the non-monotonic potential structure. The arrows in (a)–(c) denote the flow and UV directions for each case, respectively.

dimensional nature of small body plasma interactions, they nonetheless can provide insight into these important processes.

Our work presented here parallels previous theoretical work by Roussos et al. (2010), who investigated the surface charging environment of Saturn's icy, non-conducting moons. This theoretical approach was applied to the upstream plasma flow hemisphere only, but serves as a useful comparison to our results, even though the exact plasma parameters are not identical between Roussos et al. (2010) and our work here. Specifically, for aligned plasma flow and UV (the “dusk” case in Roussos et al. (2010)), the surface potentials on the four saturnian satellites are close to zero (although both positive and negative depending on the exact plasma conditions at each moon) for solar zenith angles less than  $70^\circ$  with a transition to larger, negative potentials towards the satellite limbs. Our simulation finds a similar potential curve for this case (cf., Fig. 6(a)), with the positive potential for smaller solar zenith angles in our simulation driven by the slightly higher photoemission current used here than expected at the saturnian moons. The surface potential for the  $90^\circ$  case also qualitatively matches between our work and Roussos et al. (2010), with near-zero or slightly positive potentials for solar zenith angles greater than approximately  $70^\circ$  transitioning to negative potentials on the satellite nightside. The anti-aligned case ( $180^\circ$ ) matches in a qualitative sense with Roussos et al. (2010), with slightly negative potentials at the sub-flow point transitioning to greater negative potentials near the satellite limb. The potentials for this case calculated by Roussos et al. (2010) for the specific saturnian moons often reach potentials much more negative (i.e.,  $-120$  V at the terminator for Rhea), but much of this discrepancy is driven by the

differing plasma parameters used in the two studies. Overall, however, our results here match well with the theoretical treatment of the sub-flow hemisphere of the objects.

Variation in the magnitude of the photoemission current may also affect the electrostatic plasma conditions around the object. As photoemission decreases, one would expect differences between the three modeled cases ( $0$ ,  $90$ , and  $180^\circ$ ) to diminish, as the ambient plasma becomes dominant over photoelectrons. This situation could represent airless bodies farther out in the solar system where photoemission currents are lower, although we do note that secondary electron emission may still be present which could partially mimic the effects seen here. In contrast, as the photoemission currents are increased, effects due to photoelectrons should generally increase, including larger surface charges and smaller sheaths (due to the higher local density of photoelectrons). This could potentially also affect the refilling of the plasma wake behind the object; as the sheath becomes thinner relative to the ambient plasma and object scale lengths, it may not be able to influence the surrounding electrostatic fields to the same degree seen in these simulations. Future work may also include a characterization of the various effects detailed here as a function of the ratio between the photoelectron Debye length and the plasma Debye length and also the ratio between the photoelectron Debye length and the object radius.

The treecode model presented here may also be useful in explaining observations of Rhea's plasma wake by the Cassini spacecraft (Roussos et al., 2012). The Cassini data show a surprising lack of a cold plasma density dropout in the close wake of Rhea while simultaneously observing an increase in the magnetic field

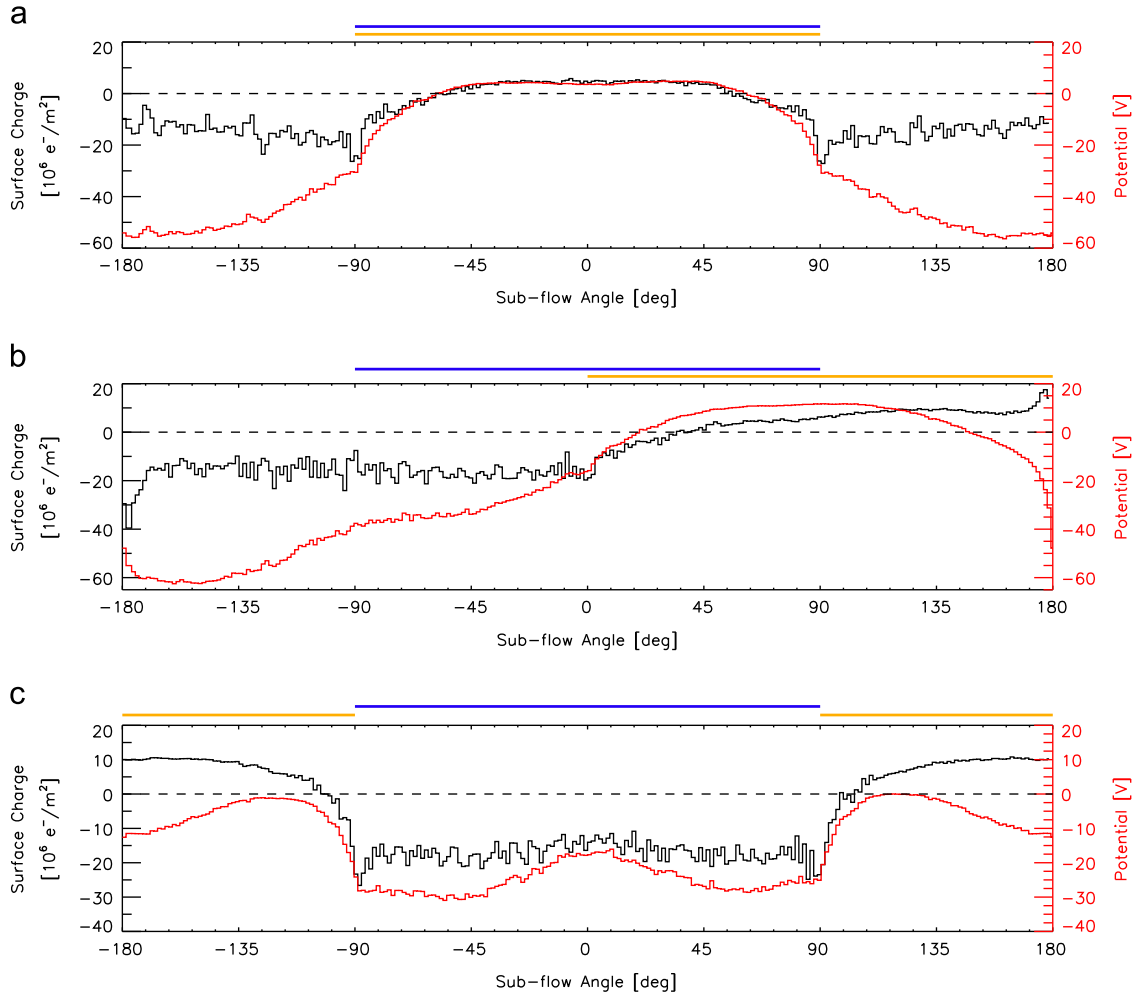


**Fig. 6.** The surface charge density (black) and surface potential (red) as a function of sub-flow angle for (a) 0°, (b) 90°, and (c) 180°. The yellow bar denotes the portion of the surface illuminated by UV radiation in each case and the blue bar denotes the portion of the surface exposed directly to plasma flow. (For interpretation of the references to color in this figure caption, the reader is referred to the web version of this paper.)

strength in the wake (plausibly due to a drop in plasma pressure). As hypothesized by Roussos et al. (2012), a cold plasma source in Rhea's wake could account for equal densities yet lower pressure. Ionospheric plasma from Rhea's oxygen/carbon dioxide exosphere (Teolis et al., 2010) is too tenuous to account for the observed plasma density, yet photoelectrons from the sunlit hemisphere of Rhea could plausibly provide enough density (Roussos et al., 2012). The specific simulation results shown here do not show that the photoelectrons replacing the entirety of the plasma density in the wake (i.e., Fig. 2(i)); however, future runs of the treecode with plasma parameters more specific to the various Rhea fly-bys and with the presence of a static background magnetic field may shed light on the ability of surface-generated photoelectrons to efficiently re-fill the plasma wake of Rhea.

While the simulations presented here have focused on an object in an un-magnetized flow, the presence of a static background magnetic field may play an important role in altering current flow to the surface, depending on both the orientation of the field and the relative size between the object radius and the electron and ion gyro-radii. For conditions in which the object radius,  $r_d$ , is smaller than both the electron and ion gyro-radii ( $r_d < r_{g,e} < r_{g,i}$ ), ambient electrons and ions in a flowing plasma can still partially access the objects wake-side surface, potentially altering the surface charge balance and resulting potential. This access will also serve to reduce the plasma density void typically found in the objects wake, as particles from the flanks of the object

gyrate completely around the object itself and enter the wake. For the intermediate case ( $r_{g,e} < d < r_{g,i}$ ), electrons are magnetized with respect to the body while ions are free to gyrate directly into the wake. Such a case is roughly typical of Earth's Moon in the solar wind, where previous observational (Nishino et al., 2009a,b; Futaana et al., 2010) and theoretical (Fatemi et al., 2012) studies have shown perpendicular entry of solar wind protons into the deep lunar wake (both electrons and ions are of course still free to enter the lunar wake along the field lines for non-parallel IMF/flow). Finally, the fully magnetized case ( $r_{g,e} < r_{g,i} < r$ ) may also prove to have interesting effects on the object surface charge distribution and wake formation, as both electrons and ions are prevented from easily accessing the downstream surface and deep wake. Each of these regimes may also have important effects on the photoelectron dynamics, which typically being colder with respect to the ambient electrons, will consequently have smaller gyroradii. Photoelectrons that escape the sheath may also be influenced by the presence of a convection electric field (for either flowing or co-rotating magnetic fields), which may lead to further asymmetries. Additionally, the interplay between a magnetized photoelectron sheath and an un-magnetized ambient plasma may significantly perturb the sheath formation. A further exploration of the electrostatic charging environment of bodies in these different regimes is of great interest and planned as future work for the treecode.

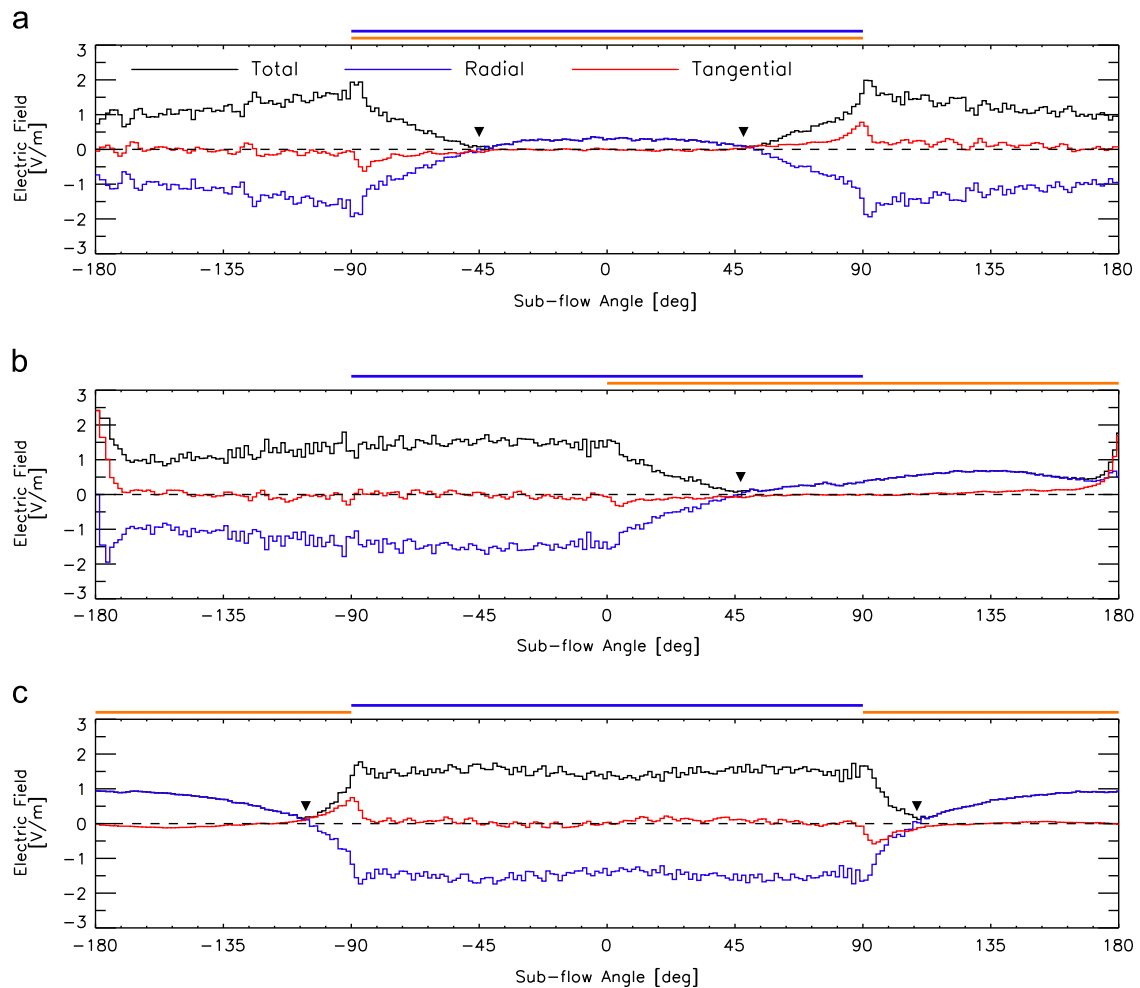


**Fig. 7.** The surface electric field radial component (blue), tangential component (red), and magnitude (black) as a function of sub-flow angle for the (a) 0°, (b) 90°, and (c) 180° cases. The yellow bar denotes the portion of the surface illuminated by UV radiation in each case and the blue bar denotes the portion of the surface exposed directly to plasma flow. Black triangles denote locations for each case where the surface electric field is approximately zero. (For interpretation of the references to color in this figure caption, the reader is referred to the web version of this paper.)

## Acknowledgments

The authors gratefully acknowledge support from NASA's Solar System Exploration Research Virtual Institute (SSERVI), grant #NNX14AG16A. This publication is SSERVI contribution #SSERVI-2014-274. The authors also acknowledge the International Space Science Institute (ISSI) for hosting a workshop series that in part inspired this work. Finally, the authors thank two reviewers for constructive comments.

## References

- Anderson, K.A., Lin, R.P., McCoy, J.E., McGuire, R.E., 1976. Measurements of lunar and planetary magnetic fields by reflection of low energy electrons. *Space Sci. Instrum.* 1, 439–470.
- Barnes, J., Hut, P., 1986. A hierarchical  $O(N \log N)$  force-calculation algorithm. *Nature* 324, 446–449.
- Birch, P.C., Chapman, S.C., 2001a. Detailed structure and dynamics in particle-in-cell simulations of the lunar wake. *Phys. Plasmas* 8 (October (10)).
- Birch, P.C., Chapman, S.C., 2001b. Particle-in-cell simulations of the lunar wake with high phase space resolution. *Geophys. Res. Lett.* 28 (January (2)), 219–222.
- Birdsall, C.K., Langdon, A.B., 1985. *Plasma Physics via Computer Simulation*. McGraw-Hill, New York.
- Christlieb, A.J., Krasny, R., Verboncoeur, J.P., Emhoff, J.W., Boyd, I.D., 2006. Grid-free plasma simulation techniques. *IEEE Trans. Plasma Sci.* 34 (2), 149–165.
- Farrell, W.M., Kaiser, M.L., Steinberg, J.T., Bale, S.D., 1998. A simple simulation of a plasma void: applications to Wind observations of the lunar wake. *J. Geophys. Res.* 103 (October (10)) 23, 653–23, 660.
- Farrell, W.M., Poppe, A.R., Zimmerman, M.I., Halekas, J.S., Delory, G.T., Killen, R.M., 2013. The lunar photoelectrons sheath: a change in trapping efficiency during a solar storm. *J. Geophys. Res.: Planets* 118.
- Farrell, W.M., Stubbs, T.J., Vondrak, R.R., Delory, G.T., Halekas, J.S., 2007. Complex electric fields near the lunar terminator: the near-surface wake and accelerated dust. *Geophys. Res. Lett.* 34.
- Fatemi, S., Holmström, M., Futaana, Y., 2012. The effects of lunar surface plasma absorption and solar wind temperature anisotropies on the solar wind proton velocity space distributions in the low-altitude lunar plasma wake. *J. Geophys. Res.* 117 (A10105), 1–13.
- Fatemi, S., Holmström, M., Futaana, Y., Barabash, S., Lue, C., 2013. The lunar wake current systems. *Geophys. Res. Lett.* 40, 1–5.
- Futaana, Y., Barabash, S., Wieser, M., Holmström, M., Bhardwaj, A., Dhanya, M.B., Sridharan, R., Wurz, P., Schaufelberger, A., Asamura, K., 2010. Protons in the near-lunar wake observed by the Sub-keV Atom Reflection Analyzer on board Chandrayaan-1. *J. Geophys. Res.* 115 (A10248).
- Grard, R.J.L., Tunaley, J.K.E., 1971. Photoelectron sheath near a planar probe in interplanetary space. *J. Geophys. Res.* 76 (10), 2498–2505.
- Gurevich, A.V., Pitaevskii, L.P., 1975. Non-linear dynamics of a rarefied ionized gas. *Prog. Aerosp. Sci.* 16, 227–272.
- Gurevich, A.V., Pitaevskii, L.P., Smirnova, V.V., 1969. Ionospheric aerodynamics. *Space Sci. Rev.* 9, 805–871.
- Halekas, J.S., Bale, S.D., Mitchell, D.L., Lin, R.P., 2005a. Electrons and magnetic fields in the lunar plasma wake. *J. Geophys. Res.* 110.
- Halekas, J.S., Delory, G.T., Brain, D.A., Lin, R.P., Fillingim, M.O., Lee, C.O., Mewaldt, R.A., Stubbs, T.J., Farrell, W.M., Hudson, M.K., 2007. Extreme lunar surface charging during solar energetic particle events. *Geophys. Res. Lett.* 34.
- Halekas, J.S., Delory, G.T., Farrell, W.M., Angelopoulos, V., McFadden, J.P., Bonnell, J.W., Fillingim, M.O., Plaschke, F., 2011. First remote measurements of lunar surface charging from ARTEMIS: evidence for nonmonotonic sheath potentials above the dayside surface. *J. Geophys. Res.* 116 (A07103).

- Halekas, J.S., Delory, G.T., Lin, R.P., Stubbs, T.J., Farrell, W.M., 2008. Lunar Prospector observations of the electrostatic potential of the lunar surface and its response to incident currents. *J. Geophys. Res.* 113 (A09102).
- Halekas, J.S., Lin, R.P., Mitchell, D.L., 2005b. Large negative lunar surface potentials in sunlight and shadow. *Geophys. Res. Lett.* 32.
- Halekas, J.S., Poppe, A., Delory, G.T., Farrell, W.M., Horányi, M., 2012. Solar wind electron interaction with the dayside lunar surface and crustal magnetic fields: evidence for precursor effects. *Earth Planets Space* 64, 73–82.
- Halekas, J.S., Poppe, A.R., McFadden, J.P., 2014. The effects of solar wind velocity distributions on the refilling of the lunar wake: ARTEMIS observations and comparisons to one-dimensional theory. *J. Geophys. Res.: Space Physics* 119.
- Harada, Y., Machida, S., Halekas, J.S., Poppe, A.R., McFadden, J.P., 2013. ARTEMIS observations of lunar dayside plasma in the terrestrial magnetotail lobe. *J. Geophys. Res.* 118, 1–8.
- Harada, Y., Machida, S., Saito, Y., Yokota, S., Asamura, K., Nishino, M.N., Tanaka, T., Tsunakawa, H., Shibuya, H., Takahashi, F., Matsushima, M., Shimizu, H., 2010. Interaction between terrestrial plasma sheet electrons and the lunar surface: SELENE (Kaguya) observations. *Geophys. Res. Lett.* 37 (L19102).
- Holmström, M., Fatemi, S., Futaana, Y., Nilsson, H., 2012. The interaction between the Moon and the solar wind. *Earth Planets Space* 64, 237–245.
- Kallio, E., 2005. Formation of the lunar wake in quasi-neutral hybrid model. *Geophys. Res. Lett.* 32 (L06107).
- McCoy, J.E., Lin, R.P., McGuire, R.E., Chase, L.M., Anderson, K.A., 1975. Magnetotail electric fields observed from lunar orbit. *J. Geophys. Res.* 80 (22), 3217–3224.
- Nakagawa, T., 2013. Ion entry into the wake behind a nonmagnetized obstacle in the solar wind: two-dimensional particle-in-cell simulations. *J. Geophys. Res.: Space Phys.* 118, 1–12.
- Nakagawa, T., Kimura, S., 2011. Role of the solar wind magnetic field in the interaction of a non-magnetized body with the solar wind: an electromagnetic 2-D particle-in-cell simulation. *Earth Planets Space* 63 (6), 477–486.
- Nishino, M.N., Fujimoto, M., Maezawa, K., Saito, Y., Yokota, S., Asamura, K., Tanaka, T., Tsunakawa, H., Matsushima, M., Takahashi, F., Terasawa, T., Shibuya, H., Shimizu, H., 2009a. Solar-wind proton access deep into the near-Moon wake. *Geophys. Res. Lett.* 36 (L16103).
- Nishino, M.N., Maezawa, K., Fujimoto, M., Saito, Y., Yokota, S., Asamura, K., Tanaka, T., Tsunakawa, H., Matsushima, M., Takahashi, F., Terasawa, T., Shibuya, H., Shimizu, H., 2009b. Pairwise energy gain-loss feature of solar wind protons in the near-Moon wake. *Geophys. Res. Lett.* 36 (L12108).
- Nitter, T., Havnes, O., Melandsø, F., 1998. Levitation and dynamics of charged dust in the photoelectron sheath above surfaces in space. *J. Geophys. Res.* 103 (A4), 6605–6620.
- Nordheim, T.A., Jones, G.H., Roussos, E., Leisner, J.S., Coates, A.J., Kurth, W.S., Khurana, K.K., Krupp, N., Dougherty, M.K., Waite, J.H., 2014. Detection of a strongly negative surface potential at Saturn's moon Hyperion. *Geophys. Res. Lett.* 41.
- Ogilvie, K.W., Steinberg, J.T., Fitzenreiter, R.J., Owen, C.J., Lazarus, A.J., Farrell, W.M., Torbert, R.B., 1996. Observations of the lunar plasma wake from the WIND spacecraft on December 27, 1994. *Geophys. Res. Lett.* 23 (10), 1255–1258.
- Poppe, A., Halekas, J.S., Horányi, M., 2011. Negative potentials above the day-side lunar surface in the terrestrial plasma sheet: evidence of non-monotonic potentials. *Geophys. Res. Lett.* 38 (L02103).
- Poppe, A., Horányi, M., 2010. Simulations of the photoelectron sheath and dust levitation on the lunar surface. *J. Geophys. Res.* 115 (A08106).
- Poppe, A.R., Fatemi, S., Halekas, J.S., Holmström, M., Delory, G.T., 2014. ARTEMIS observations of extreme diamagnetic fields in the lunar wake. *Geophys. Res. Lett.*
- Poppe, A.R., Halekas, J.S., Delory, G.T., Farrell, W.M., Angelopoulos, V., McFadden, J.P., Bonnell, J.W., Ergun, R.E., 2012a. A comparison of ARTEMIS observations and particle-in-cell modeling of the lunar photoelectron sheath in the terrestrial magnetotail. *Geophys. Res. Lett.* 39 (L01102).
- Poppe, A.R., Halekas, J.S., Samad, R., Sarantos, M., Delory, G.T., 2013. Model-based constraints on the lunar exosphere derived from ARTEMIS pick-up ion observations in the terrestrial magnetotail. *J. Geophys. Res.* 118, 1–13.
- Poppe, A.R., Piquette, M., Likhanskii, A., Horányi, M., 2012b. The effect of surface topography on the lunar photoelectron sheath and electrostatic dust transport. *Icarus* 221, 135–146.
- Roussos, E., Kollman, P., Krupp, N., Paranicas, C., Krimigis, S.M., Mitchell, D.G., Persoon, A. M., Gurnett, D.A., Kurth, W.S., Krieger, H., Simon, S., Khurana, K.K., Jones, G.H., Wahlund, J.-E., Holmberg, M.K.G., 2012. Energetic electron observations of Rhea's magnetospheric interaction. *Icarus* 221, 116–134.
- Roussos, E., Krupp, N., Krüger, H., Jones, G.H., 2010. Surface charging of Saturn's plasma-absorbing moons. *J. Geophys. Res.* 115 (A08225).
- Roussos, E., Müller, J., Simon, S., Bösswetter, A., Motschmann, U., Krupp, N., Fränz, M., Woch, J., Khurana, K.K., Dougherty, M.K., 2008. Plasma and fields in the wake of Rhea: 3-D hybrid simulation and comparison with Cassini data. *Ann. Geophys.* 26, 619–637.
- Samir, U., Wright Jr., K.H., Stone, N.H., 1983. The expansion of a plasma into a vacuum: basic phenomena and processes and applications to space plasma physics. *Rev. Geophys.* 21, 1631–1646.
- Simon, S., Saur, J., Neubauer, F.M., Motschmann, U., Dougherty, M.K., 2009. Plasma wake of Tethys: hybrid simulations versus Cassini MAG data. *Geophys. Res. Lett.* 36 (L04108).
- Tanaka, T., et al., 2009. First in situ observation of the Moon-originating ions in the Earth's Magnetosphere by MAP-PACE on SELENE (KAGUYA). *Geophys. Res. Lett.* 36 (L22106).
- Teolis, B.D., Jones, G.H., Miles, P.F., Tokar, R.L., Magee, B.A., Waite, J.H., Roussos, E., Young, D.T., Crary, F.J., Coates, A.J., Johnson, R.E., Tseng, W.-L., Baragiola, R.A., 2010. Cassini finds an oxygen-carbon dioxide atmosphere at Saturn's icy Moon Rhea. *Science* 330, 1813–1815.
- Trávníček, P., Hellinger, P., Schriver, D., Bale, S.D., 2005. Structure of the lunar wake: two-dimensional global hybrid simulations. *Geophys. Res. Lett.* 32 (L06102).
- Whipple, E.C., 1981. Potentials of surfaces in space. *Rep. Prog. Phys.* 44.
- Wurz, P., Rohner, U., Whitby, J.A., Kolb, C., Lammer, H., Dobnikar, P., Martín-Fernández, J.A., 2007. The lunar exosphere: the sputtering contribution. *Icarus* 191, 486–496.
- Xie, L.H., et al., 2013. Three-dimensional MHD simulation of the lunar wake. *Science China Earth Sciences* 56 (2), 330–338, <http://dx.doi.org/10.1007/s11430-012-4383-6>.
- Zimmerman, M.I., Farrell, W.M., Poppe, A.R., 2014. Grid-free 2D plasma simulations of the complex interaction between the solar wind and small, near-earth asteroids. *Icarus* 238, 77–85.